



BASIC SCIENCE

Nanomedicine: Nanotechnology, Biology, and Medicine 35 (2021) 102392



Original Article

nanomedjournal.com

Superparamagnetic iron oxide–gold nanoparticles conjugated with porous coordination cages: Towards controlled drug release for non-invasive neuroregeneration

Muzhaozi Yuan, PhD^{a,*}, Tian-Hao Yan, BSc^b, Jialuo Li, PhD^b, Zhifeng Xiao, BSc^b, Yu Fang, PhD^{c,*}, Ya Wang, PhD^{a,e,f,**}, Hong-Cai Zhou, PhD^{b,*}, Jean-Philippe Pellois, PhD^{b,d}

^aJ. Mike Walker '66 Department of Mechanical Engineering, Texas A&M University, College Station, TX, USA because of Chemistry, Texas A&M University, College Station, TX, USA

^cState Key Laboratory for Chemo/Bio-Sensing and Chemometrics, College of Chemistry and Chemical Engineering, Hunan University, Changsha, Hunan, P. R. China

^dDepartment of Biochemistry and Biophysics, Texas A&M University, College Station, TX, USA
^cDepartment of Electrical and Computer Engineering, Texas A&M University, College Station, TX, USA
^fDepartment of Biomedical Engineering, Texas A&M University, College Station, TX, USA

Abstract

This paper reports a smart intracellular nanocarrier for sustainable and controlled drug release in non-invasive neuroregeneration. The nanocarrier is composed by superparamagnetic iron oxide-gold (SPIO-Au) core-shell nanoparticles (NPs) conjugated with porous coordination cages (PCCs) through the thiol-containing molecules as bridges. The negatively charged PCC-2 and positively charged PCC-3 are compared for intracellular targeting. Both types result in intracellular targeting via direct penetration across cellular membranes. However, the pyrene (Py)-PEG-SH bridge enabled functionalization of SPIO-Au NPs with PCC-3 exhibits higher interaction with PC-12 neuron-like cells, compared with the rhodamine B (RhB)-PEG-SH bridge enabled case and the stand-alone SPIO-Au NPs. With neglectable toxicities to PC-12 cells, the proposed SPIO-Au-RhB(Py)-PCC-2(3) nanocarriers exhibit effective drug loading capacity of retinoic acid (RA) at 13.505 µg/mg of RA/NPs within 24 h. A controlled release of RA is achieved by using a low-intensity 525 nm LED light (100% compared to 40% for control group within 96 h).

© 2021 Elsevier Inc. All rights reserved.

Effective intracellular delivery to the central nervous system remains a major challenge for therapeutic agents, including genes, 1,2 growth factors, 3,4 and other neuroprotective drugs. 5

The pharmacological effectiveness of these agents usually requires the continuous intracellular release of them. Additionally, many agents have restrictions to reach the intracellular

Abbreviations: RA, retinoic acid; NPs, nanoparticles; SPIO, superparamagnetic iron oxide; LED, light emitting diode; PCCs, porous coordination cages; SPIO-Au, superparamagnetic iron oxide-gold; RhB, rhodamine B; Py, pyrylium; PEG, polyethylene glycol; DMEM, Dulbecco's Modified Eagle's Medium (DMEM); DI, deionized water; DMSO, dimethyl sulfoxide; TEM, transmission electron microscopy; ICP-MS, inductively coupled plasma mass spectrometry; PBS, phosphate-buffered saline; ANOVA, analysis of variance.

Funding sources: U.S. National Science and Foundation (CAREER 1751435, Y.W.; GCR 2021081, Y.W.)

U.S. National Institute of General Medical Sciences (R01GM110137, J.-P.P.)

Cancer Prevention and Research Institute of Texas (RP190655, J.-P.P.)

https://doi.org/10.1016/j.nano.2021.102392

1549-9634/© 2021 Elsevier Inc. All rights reserved.

The authors declare no conflict of interest.

^{*} Corresponding authors.

^{**} Correspondence to: Y. Wang, J. Mike Walker '66 Department of Mechanical Engineering, Texas A&M University, College Station, TX, USA. *E-mail addresses:* muzhaozi.yuan@tamu.edu (M. Yuan), thyan426@tamu.edu (T.-H. Yan), lijialuo@tamu.edu (J. Li), xiao@tamu.edu (Z. Xiao), yu.fang@hnu.edu.cn (Y. Fang), ya.wang@tamu.edu (Y. Wang), zhou@chem.tamu.edu (H.-C. Zhou), pellois@tamu.edu (J.-P. Pellois).

targets with sufficient concentrations. 6 Among these therapeutic agents, retinoic acid (RA) is known for their neuroprotective effects⁷ by promoting dopaminergic neuronal survival, growth,⁸ differentiation, 7,9 and synaptic transmission. 10 However, the administration of RA is challenging because of its short half-life, low water solubility and rapid metabolization rate in cells. 1 Particularly, the release of RA has to be carefully designed to avoid side-effects due to the high concentration. 7, 12, 13 A promising solution to achieve sustained intracellular drug release over time is to use the colloidal nanoparticles (NPs) as smart carriers of RA, such as polymeric NPs, 11,14,15 dendrimer coated superparamagnetic iron oxide (SPIO) NPs, 16 and diblock copolymers. 17 The surface function of these NPs can be modified to improve BBB targeting and extend the circulation time of RA.6,18 However, they either lack sufficient control for RA release or are too complicated to be assembled efficiently. External stimuli such as light 19,20 and alternating magnetic fields^{21,22} have been studied to control the release of RA and other drugs. However, their release rate is too fast to be practical (100% release after several minutes). In this paper, we report a novel facile-assembled smart nanocarrier facilitating the intracellular release of RA and potentially, many other drugs at a well-controlled rate in pharmacological practice using external stimuli, such as light emitting diode (LED).

With demonstrated tunable drug loading capacities, the porous coordination cages (PCCs) possess intrinsic porosity inside the hollow structure constructed by metal clusters as vertices and organic panel ligands as faces. ^{23–25} Their electronic and chemical properties can be tuned by manipulating the surface functional groups and coordination sites. 23-25 For example, the net-charge of PCCs can be modified from neutral to negative by replacing the tert-butyl groups with anionic sulfate groups. Therefore they can be used to carry hydrophobic guest molecules with different types of charges through strong electrostatic interactions. ^{26–28} Recently, we have developed customized PCCs for versatile hydrophobic guest molecule encapsulation: in particular, PCC-2 with negative net-charge to encapsulate cationic dye (Rhodamine B) and PCC-3 with positive net-charge and stronger hydrophobicity than PCC-2 to encapsulate hydrophobic dye (Nile Red). 26 However, the invitro and in-vivo imaging of such PCCs is barely possible because the contrast of these PCCs is too low to be used for bioimaging. It is also challengeable to realize the remotely controlled drug release from PCCs.

Lately, another promising nanocarrier, superparamagnetic iron oxide-gold (SPIO-Au) core-shell NPs, has attracted lots of attention due to their excellent cellular uptake ability, ^{29,30} high dual-mode contrast for bioimaging, ^{31,32} plasmonic properties, ³³ magnetic properties, ^{34–36} biocompatibility, ^{37–41} biostabilities, ^{31,38} and tunable surface function. ⁴² Besides, Au NPs have shown benefits for neuronal regeneration and recovery. ^{43–45}

These aforementioned advantages of SPIO-Au NPs and PCCs motivate us to explore the synergistic function of SPIO-Au NPs conjugated with PCCs for controlled intracellular drug delivery. We use the thiol-containing molecules (rhodamine B(RhB)/pyrene(Py)-polyethylene glycol(PEG)-SH) as bridges for their functionalization, as shown in Figure 1. More specifically, on one end of the thiol-containing molecule, –SH links to the

surface of Au NPs by the strong Au–S linkage. On the other end, RhB attracts PCC-2, primarily by electrostatic attraction, and Py attracts PCC-3 solely by hydrophobic interactions. ⁴⁶ We hypothesized that SPIO-Au-RhB-PCC-2 and SPIO-Au-Py-PCC-3 NPs would possess the enhanced efficiency of intracellular targeting with strong magnetic properties, the effectiveness of drug loading with specified electrical and hydrophobic properties, and the controllability of drug release via light. We also hypothesized that by using LED stimulation, the sustained release rate of drugs over a prolonged time period can be controlled to realize a more effective delivery within the short half-lives of these NPs.

In this work, we tuned the surface charge of SPIO-Au-Py-PCC-3 NPs so that RA molecules can be attracted to PCCs by electrostatic interactions. The hydrophobic interaction further enhanced the RA encapsulation into PCCs. We observed the intracellular uptake of SPIO-Au-RhB-PCC-2 and SPIO-Au-Py-PCC-3 NPs into PC-12 cells with neglectable toxicity. We evaluated the interaction of different thiol bridges: Py-PEG-SH and RhB-PEG-SH with cells using TEM and elemental analysis. Importantly, we quantified the loading capacity of RA using SPIO-Au-Py-PCC-3 NPs, and confirmed that LED light promotes the release of RA in Dulbecco's Modified Eagle's Medium (DMEM).

Methods

Functionalization of SPIO-Au NPs with RhB/Py-PEG-SH and PCCs

SPIO-Au NPs²⁹ and PCCs²⁶ were prepared using previously developed methods (Supplementary Materials). SPIO-Au NPs were then functionalized with RhB-PEG-SH (FL045003-1K, Biochempeg Scientific Inc.) and Py-PEG-SH (PG2-PNTH-2K, Nanocs Inc.), respectively, by suspending 366 µg of SPIO-Au NPs in 1 mL of deionized (DI) water with 100 µg of RhB-PEG-SH/Py-PEG-SH at room temperature for 24 h. Then the RhB/Py functionalized SPIO-Au NPs (named as SPIO-Au-RhB or SPIO-Au-Py) were isolated by centrifugation and washed by water for at least 3 times. SPIO-Au-RhB NPs were then suspended in 1 mL of dimethyl sulfoxide (DMSO) solution and mixed with 25 µg of PCC-2 at room temperature for 24 h, followed by the centrifuging and washing process for at least 3 times using DMSO. The resultant was named as SPIO-Au-RhB-PCC-2. On the other hand, SPIO-Au-Py NPs were suspended in DI water and mixed with 10 µg of PCC-3 at room temperature for 24 h, followed by the centrifuging and washing process for at least 3 times using DI water. The resultant was named as SPIO-Au-Py-

To adjust the surface charge of SPIO-Au-Py-PCC-3 NPs for the purpose of loading RA, 0.175 M of acetic acid at the volume of 20, 100, 200, and 500 μL was added to every 127 μg of SPIO-Au NPs for 5 min to neutralize the surface charge of the standalone SPIO-Au NPs. The NPs were then centrifuged and washed 3 time to remove the extra acetic acid. After that, the NPs were functionalized by Py and PCC-3 following the same steps mentioned above.

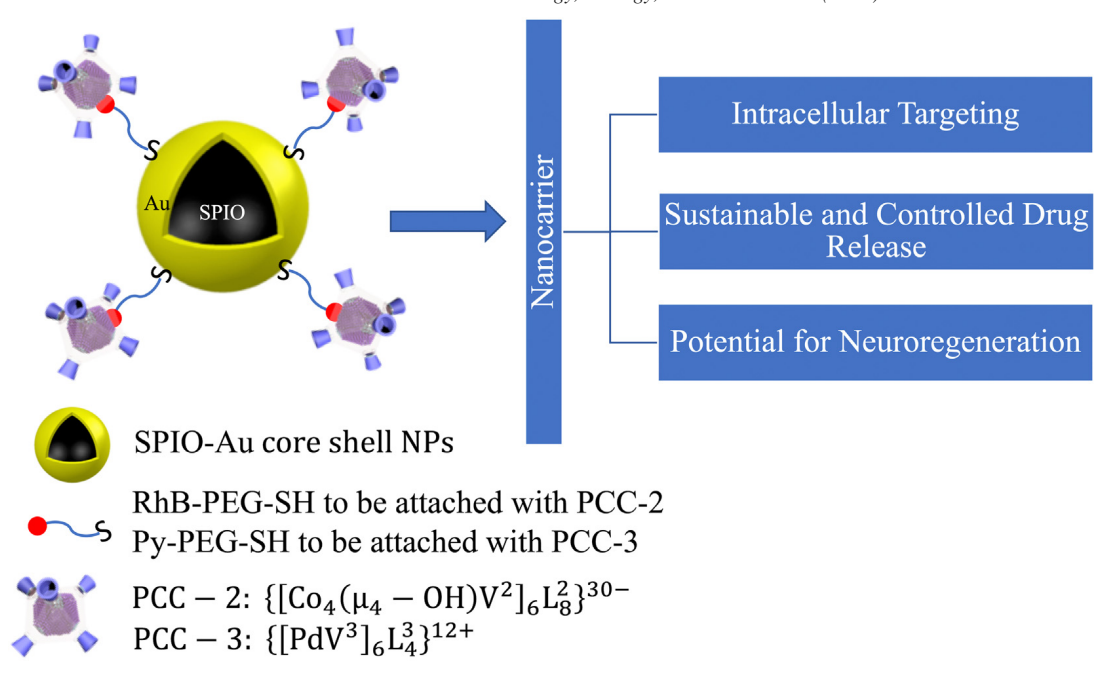


Figure 1. Schematic illustration of the nanocarrier.

The characterization of SPIO-Au NPs functionalized with RhB/ Py-PEG-SH and PCCs

To observe the morphology of the synthesized SPIO-Au NPs, the transmission electron microscopy (TEM) imaging was performed on FEI Tecnai G2 F20 S-Twin Field-Emission Scanning Transmission Electron Microscope at an operating voltage of 200 kV. Briefly, $100~\mu L$ of each sample were dropped onto a 400-mesh copper grid (Electron Microscopy Sciences, Hatfield, PA) and then left to dry in the air.

To verify the functionalization of SPIO-Au NPs with RhB-PEG-SH, the light absorption spectra of SPIO-Au NPs before and after the functionalization with RhB-PEG-SH were recorded at wavelengths between 350 and 1000 nm at room temperature with a SHIMADZU UV-2450 spectrophotometer (Shimadzu Corp.). To verify the functionalization of SPIO-Au NPs with Py-PEG-SH, the fluorescence signal of SPIO-Au-Py NPs was recorded at 339 nm excitation at room temperature with a SHIMADZU RF-5301PC Spectrofluorophotometer (Shimadzu Corp.). The zeta potential and the hydrodynamic diameter of SPIO-Au NPs with different functionalizations in DI water and DMEM were measured using a Malvern Zetasizer Nano ZS (Malvern Instruments Inc.).

The quantification of elemental composition of SPIO-Au NPs and SPIO-Au-RhB(Py)-PCC-2(3) NPs

The SPIO-Au NPs before and after functionalization with PCCs were digested in mineral acid. 2% nitric acid was used as an analytical matrix for inductively coupled plasma mass spectrometry (ICP-MS). In detail, the NPs were centrifuged with the removal of top solution and digested by a mixture of hydrochloric acid (0.3 mL, ~30%) and nitric acid (1.1 mL, ~65%). The samples were then diluted into 2% nitric acid and

tested on the PerkinElmer NexION 300D Inductively Coupled Plasma Mass Spectrometer (PerkinElmer, Inc.).

The quantification of Au amount that interacted with cells

PC-12 cells were cultured (protocol in Supplementary Materials) and seeded into Corning® BioCoatTM 24-well plates precoated with collagen type IV and incubated for 1 day. Then the cells were washed with phosphate-buffered saline (PBS) and incubated in medium supplemented with SPIO-Au NPs with different surface functionalizations at the concentration of 20 μg mL $^{-1}$. After 1 and 2 days, the cells were washed with PBS for 3 times. This step was to make sure of the removal of the contamination of unassociated, unattached, or free NPs outside the cells. Then the cells were digested and the amount of Au in each sample was quantified using ICP-MS according to the previous digestion steps.

Cell viability via flow cytometry

PC-12 cells were seeded into Corning® BioCoatTM 24-well plates precoated with collagen type IV and incubated for 1 day. Then the cells were washed with PBS and incubated with medium containing SPIO-Au NPs (20 µg mL⁻¹) with different surface functionalizations. After 1, 3 and 5 days, the media were removed and the dead and total cells were stained with SYTOX Green (1:30,000 dilution from stock solution, Invitrogen) and SYTO 59 Red (1:1000 dilution from stock solution, Invitrogen), respectively, for 30 min with protection from light. Then the staining solution was removed. The cells were washed 2-3 times using serum-free media, trypsinized and resuspended in serum-free media for fluorescence measurement through BD Accuri C6 flow cytometer equipped with FL1 detector (553 nm) and FL 3

detector (670 nm). All data were acquired at a flow rate of $14 \,\mu\text{L}$ min⁻¹ with a minimum of 20,000 events detected.

TEM analysis revealing the cellular uptake

PC-12 cells were seeded onto 35 mm Permanox petri dishes at a density of $2*10^5$ cells per dish and incubated for 24 h. Then the media were replaced by growth medium containing SPIO-Au NPs (20 μg mL⁻¹) with different surface functionalizations. After 24 h of incubation, cells were rinsed with serum-free media and 0.1 M cacodylate buffer. Cells were then fixed, dehydrated, embedded, sectioned (Supplementary Materials), and analyzed using an FEI transmission electron microscope, at an accelerating voltage of 80 kV.

Determination of the loading efficiency and the release profile of RA

400 μL of RA solution in DMSO was added to 300 μL of SPIO-Au-Py-PCC-3 solution with the concentration of 1274.7 μg mL $^{-1}$ (SPIO-Au) drop by drop with ultrasonication for 5 min to enhance the drug encapsulation. The solution was left in room temperature for 24 h. Then the solution was centrifuged, and separated to get the precipitate as drug-loaded NPs. The RA absorption spectra of the standard RA solutions (4.69-75 μg mL $^{-1}$; R2=0.9995) and the top solution was measured at 350 nm using the SHIMADZU UV-2450 spectrophotometer (Shimadzu Corp.). The concentration of the free unbounded RA in the top solution was calculated using the standard curve according to the Beer-Lambert law that there is a linear relationship between the light absorbance and the concentration. The payload rate of NPs was calculated using the following equation:

$$Payload \ rate = \frac{Mass \ of \ RA \ loaded \ by \ NPs}{mass \ of \ NPs} \tag{1}$$

The drug release profile of RA loaded SPIO-Au-Py-PCC-3 NPs was evaluated in cell-free DMEM. The NPs were dispersed in 100 µL of DMEM and then introduced into a micro dialysis tube (Molecule weight cut-off: 12 kDa). Dialysis tube was then inserted into a microcentrifuge tube containing 1.3 ml of the fresh DMEM. Then the LED light at the intensity of 1.9 mW/cm² was immediately applied to the dialysis tube for 30 min of illumination. At the time point of 0.5, 1, 2, 4, 8, 12, 24, 48, 72 h and 96 h, the whole released media were exchanged with fresh media to maintain the sink condition, and measured by ultraviolet measurements at 350 nm. The RA content in the medium was determined according to the standard curve of RA solutions.

Statistical analysis

Statistical analysis was performed by using the analysis of variance (ANOVA) with Tukey post-hoc test to assess SPIO-Au treated groups with different surface functionalizations. A *P* value less than 0.05 was considered as a significant difference.

Results

The functionalization of SPIO-Au NPs with the thiol group

The TEM images (Figure 2) showed the SPIO cores (D: 11.7 ± 1.7 nm) before the Au coating, and the SPIO-Au NPs (D: 19.6 \pm 3.7 nm) with a quasi-spherical shape and a narrow-size distribution. The SPIO-Au NPs were then functionalized with RhB-PEG-SH and Py-PEG-SH, respectively. A peak shift from 524 nm to 532 nm was found in the UV-vis light absorbance spectra of SPIO-Au NPs by the functionalization with RhB-PEG-SH (Figure 3, A), indicating the attachment of RhB-PEG-SH (absorbance peak at 556 nm) onto the surface of SPIO-Au NPs. A typical fluorescence emission spectrum which came from the Py group 47 confirmed the successful functionalization of SPIO-Au NPs with Py-PEG-SH (Figure 3, B). However the fluorescence signal could hardly be detected for RhB-PEG-SH functionalized NPs due to the strong fluorescence quenching effect of Au. The different quenching effects of SPIO-Au NPs on Py and RhB were possibly due to the different PEG chain lengths of Py-PEG-SH (2 kDa) and RhB-PEG-SH (1 kDa). It was reported that the longer PEG chain between the fluorescence dye and Au NPs led to the weaker fluorescence quenching effect. 48,49 Additionally, the zeta potential was changed from -39.9 ± 0.1 mV to -35.4 ± 0.7 mV by the functionalization of SPIO-Au NPs by Py-PEG-SH, and it was also changed from -39.9 ± 0.1 mV to -16.0 ± 3.2 mV by the functionalization of SPIO-Au NPs by RhB-PEG-SH. This change confirmed the replacement of the weakly attached negative citrate molecules by the neutral Py-PEG-SH groups and the positive RhB-PEG-SH groups, respectively, due to the strong Au-S linkage (Table 1). The peak value of hydrodynamic diameter distribution was also changed from 43 nm to 59 nm and 190 nm by the functionalization of SPIO-Au NPs with RhB-PEG-SH and Py-PEG-SH, respectively (Figure 3, C and D). The much larger hydrodynamic diameter of SPIO-Au-Py NPs than SPIO-Au-RhB NPs was possibly due to the larger molecular weight of Py-PEG-SH compared to RhB-PEG-SH.

The functionalization of the SPIO-Au-RhB and SPIO-Au-Py NPs with PCC-2 and PCC-3

Given that the SPIO-Au-RhB NPs and SPIO-Au-Py NPs had negative surface charge, modifying them with negatively charged PCC-2 and positively charged PCC-3 would significantly change the overall net-charge of them. By functionalizing with PCC-2, the zeta potential of SPIO-Au-RhB NPs was changed from -16.0 ± 3.2 mV to -29.5 ± 1.9 mV, indicating the successful attachment of negatively charged PCC-2. By functionalizing with PCC-3, the zeta potential of SPIO-Au-Py NPs was changed from -35.4 ± 0.7 mV to -16.9 ± 4.6 mV, strongly suggesting that positively charged PCC-3 cages were on board (Table 1). The significantly increased hydrodynamic diameter (Figure 3, C, D and Figure S1) again confirmed the successful attachment of PCC-2 and PCC-3 onto SPIO-Au-RhB and SPIO-Au-Py NPs. The element analysis confirmed a 32.3% (mass) of Fe and a 67.7% (mass) of Au in the stand-alone SPIO-Au NPs, as well as a 0.3% (mass) of Pd (exclusively existed in PCC-3) and 3.3% (mass) of Co (exclusively existed in PCC-2) in SPIO-Au-Py-PCC-3 and SPIO-Au-RhB-PCC-2 NPs, respectively, which further demonstrated the

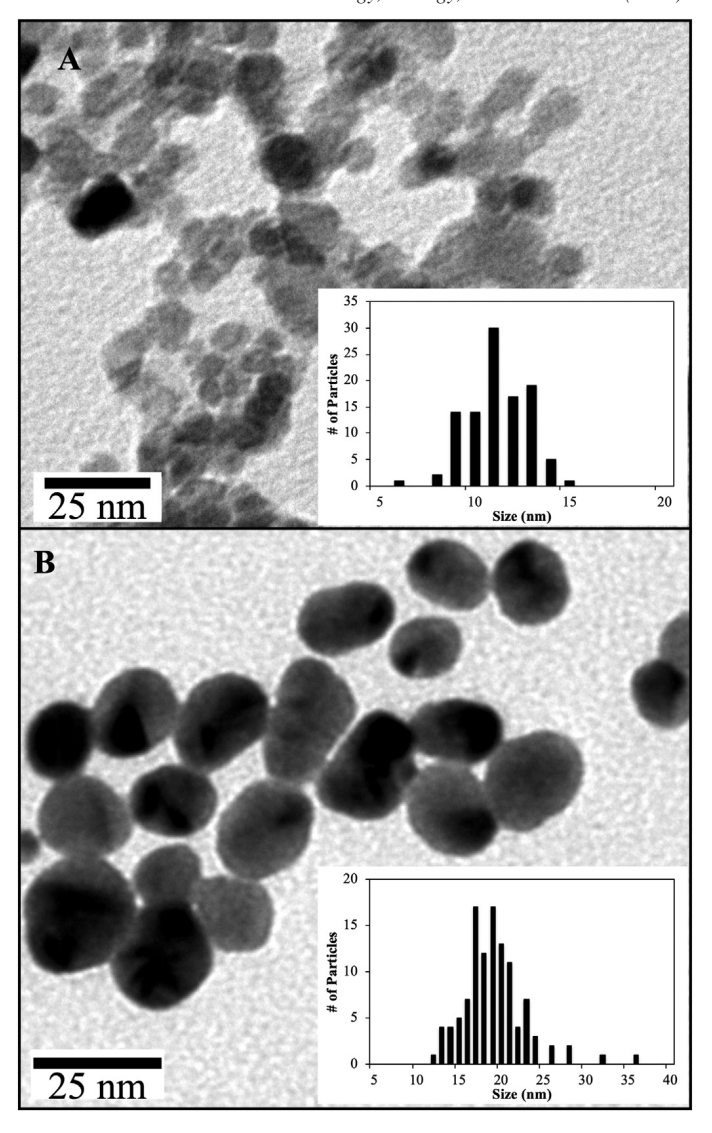


Figure 2. The TEM images of the NPs. (A) SPIO NPs $(11.7 \pm 1.7 \text{ nm})$; (B) SPIO-Au NPs $(19.6 \pm 3.7 \text{ nm})$.

successful functionalization of SPIO-Au-RhB and SPIO-Au-Py NPs with PCC-2 and PCC-3. According to the molar ratio of Pd: PCC-3 (6:1) and Co:PCC-2 (24:1), the number of PCC-3 and PCC-2 per NPs was estimated to be 30 and 352, respectively (Table 2). One possible reason why the number of PCC-2 and PCC-3 was so different was that the longer PEG chain of Py-PEG-SH than RhB-PEG-SH restricted the attached number of Py-PEG-SH onto SPIO-Au NPs, which further restricted the number of PCC-3 per SPIO-Au NPs. It was also possible that the attractive interactions between SPIO-Au-RhB and PCC-2 were stronger than those between SPIO-Au-RhB and PCC-3: both the electrostatic attraction and hydrophobic attraction existed between PCC-2 (negative charge) and RhB (positive charge), while only hydrophobic interaction existed between PCC-3 (positive charge) and Py (neutral charge).

To further adjust the surface charge of SPIO-Au-Py-PCC-3 NPs from negative to positive for the purpose of loading negatively charged RA, the acetic acid was used to neutralize the surface charge of the stand-alone SPIO-Au NPs at first. By

adjusting the acid amount from 20 to 500 μ L, the zeta potential of SPIO-Au NPs was changed from –36.3 to –12.8 mV, showing the process of neutralization of the negatively charged citrate ligands at the surface of SPIO-Au NPs (Figure 4, A). It could be hypothesized that the zeta potential of SPIO-Au-Py-PCC-3 NPs could be adjusted by choosing the appropriate amount of acid to neutralize part of the negatively charged citrate ligand before the partial replacement of citrate by Py-PEG-SH at the surface of SPIO-Au NPs. Results showed that the zeta potential of SPIO-Au NPs was changed from –36.3 to –23.3 mV by acid neutralization (100 μ L acid, Figure 4, B). It was then changed to –9.3 mV by Py functionalization and was further changed to 18 mV by PCC-3 functionalization, which was capable to attract RA by the strong electrostatic interaction.

To further examine the stability of SPIO-Au, SPIO-Au-Py-PCC-3 and SPIO-Au-RhB-PCC-2 NPs, we dispersed them in DI water and DMEM to measure their zeta potential and hydrodynamic diameters at 25 and 37 °C, respectively. In

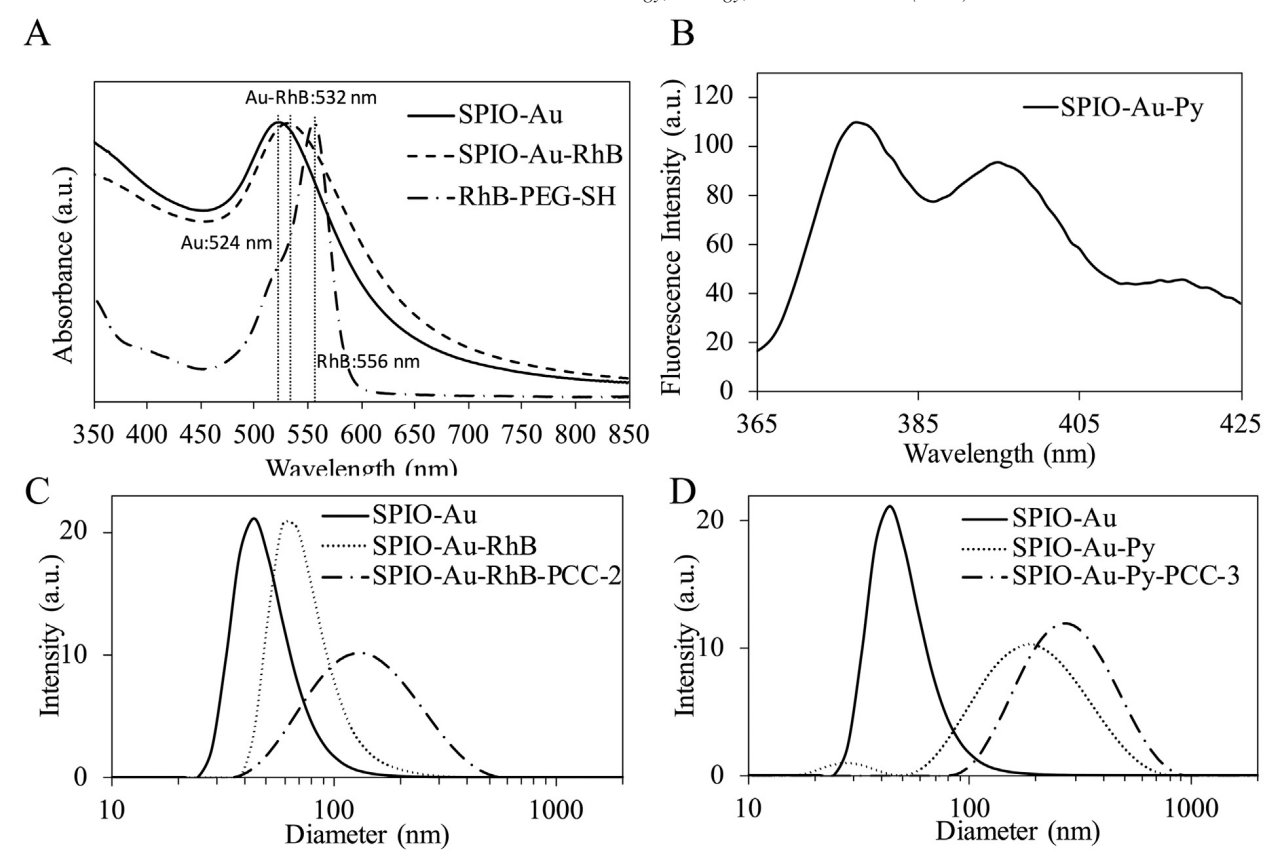


Figure 3. Light absorbance and fluorescence measurement: (A) The normalized UV-vis spectra of the stand-alone SPIO-Au NPs, the SPIO-Au NPs functionalized with RhB-PEG-SH and the stand-alone RhB-PEG-SH (the peak absorbance value as 1). (B) The fluorescence spectrum of the SPIO-Au NPs functionalized with Py-PEG-SH. (C) The intensity distribution of hydrodynamic diameters of SPIO-Au NPs before and after the RhB-PEG-SH functionalization in DI water at 25 °C. (D) The intensity distribution of hydrodynamic diameters SPIO-Au NPs before and after the Py-PEG-SH functionalization in DI water at 25 °C.

Table 1
The zeta potential measurement for SPIO-Au NPs with different functional groups dispersed in DI water at 25 °C and pH=5.43.

	SPIO-Au	SPIO-Au-Py	SPIO-Au-Py-PCC-3	SPIO-Au-RhB	SPIO-Au-RhB-PCC-2
Zeta potential [mV]	-39.9 ± 0.1	-35.4 ± 0.7	-16.9 ± 4.6	-16.0 ± 3.2	-29.5 ± 1.9

Table 2 ICP-MS results showing the relative mass composition for the stand-alone SPIO-Au, SPIO-Au-Py-PCC-3 and SPIO-Au-RhB-PCC-2 NPs. (Original dataset is listed in Table S3.)

Group abbreviations	Fe [%]	Au [%]	Co [%]	Pd [%]	Number of PCCs per NP
SPIO-Au	32.3	67.7	N/A	N/A	N/A
SPIO-Au-Py-PCC-3	24.7	75.0	N/A	0.3	30
SPIO-Au-RhB-PCC-2	22.0	74.7	3.3	N/A	352

DMEM, the zeta potential maintained stable, indicating the physiological temperature did not affect the surface charge properties of these NPs in medium. However, in DI water, the zeta potential changed slightly at 37°C compared to that at 25 °C. We also found that, at the same temperature, the zeta potentials of SPIO-Au and SPIO-Au-RhB-PCC-2 NPs in DMEM were less negative than them in DI water, while the zeta potentials of SPIO-Au-Py-PCC-3 NPs were more negative in DMEM than them in DI water (Table 3). This difference was possibly due to the absorption of different cations and anions in DMEM onto

PCC-3 (locally exhibiting positive net-charge and may attract anions to change zeta potential towards negative), PCC-2 (locally exhibiting negative net-charge and may attract cations to change zeta potential towards 0), and NPs (exhibiting negative charge and may attract cations to change zeta potential towards 0). ⁴¹ We also found that the hydrodynamic diameters of all NPs in DMEM were much larger than those in DI water (Table S2). This may also be caused by the strong absorption of cation and anions onto PCCs and the change in zeta potential which reflected the surface charge properties of NPs. The less negative

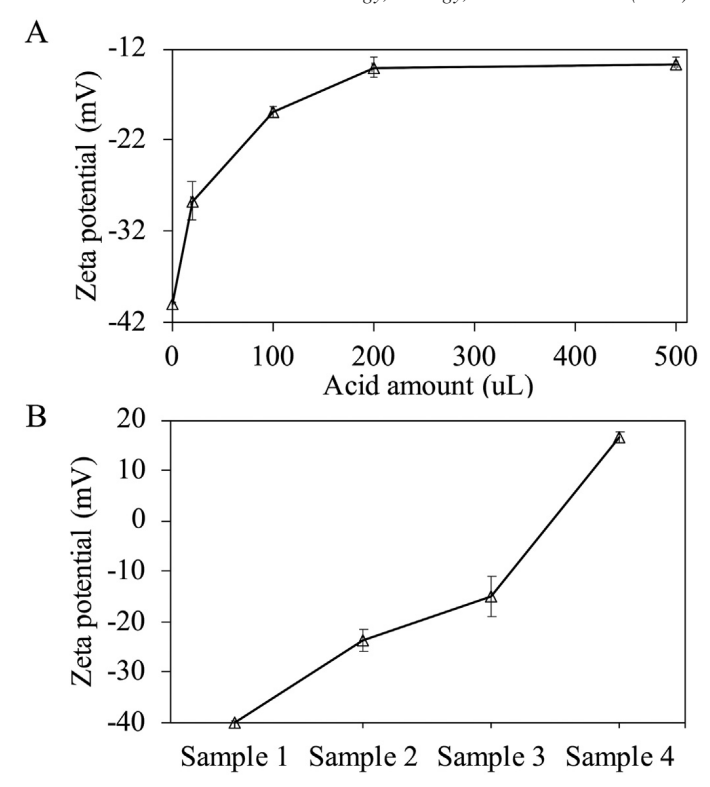


Figure 4. The zeta potential measurement of (A) SPIO-Au NPs with acid neutralization for acetic acid amount increased from 20 to $500\,\mu\text{L}$ at the concentration of 0.175 mol/L for every 127 µg of SPIO-Au NPs. (B) SPIO-Au NPs with acid neutralization and further functionalization with Py and PCC-3 showing that the zeta potential was changed from negative to positive. (Sample 1: original SPIO-Au; sample 2: acid washed SPIO-Au; sample 3: acid washed SPIO-Au-Py; sample 4: acid washed SPIO-Au-Py-PCC-3. The pH value for all the samples in DI water was around 5.47.)

Table 3
The zeta potential of SPIO-Au NPs with different functional groups in DI water and DMEM medium, measured at 25 °C and 37 °C (unit: mV).

	Water (pH = 5.43)		DMEM medium (pH = 7.06)	
	25 °C	37 °C	25 °C	37 °C
SPIO-Au	-41.9 ± 1.6	-37.5 ± 0.7	-11.7 ± 0.5	-11.37 ± 0.6
SPIO-Au-Py-PCC-3	-2.8 ± 1.3	-5.43 ± 1.4	-9.9 ± 0.3	-9.85 ± 0.8
SPIO-Au-RhB-PCC-2	-29.5 ± 1.9	-18.67 ± 0.2	-14.6 ± 0.3	-14.6 ± 1.0

zeta potential in DMEM indicated the weaker surface charge of NPs and the weaker repulsive electrostatic forces between NPs, which may have led to the agglomeration of NPs.

Cellular uptake analysis

The cellular uptake of SPIO-Au, SPIO-Au-Py-PCC-3 and SPIO-Au-RhB-PCC-2 NPs was verified at the concentration of 20 μg mL⁻¹ by TEM analysis. More SPIO-Au-Py-PCC-3 NPs were found inside the cells compared with another two cases, implying the promotional effect of Py-PEG-SH enabled PCC-3 functionalization on cellular uptake of SPIO-Au NPs. For all three cases, NPs were found successfully internalized into the PC-12 cells and located in the cytoplasm, rather than the nucleus.²⁵ No NPs were found located in the endosome or bounded by any membrane, indicating the possible nonendocytic uptake of NPs into the cells (Figure 5). Such an uptake approach was also reported by using TiO₂ NPs (200 nm),

gold NPs (39 nm) and polystyrene microspheres (up to 2 μ m) via direct penetration into cells. ^{50–52} The cellular uptake pathway could be affected by the concentration of Au NPs: lower concentration (10 μ g mL⁻¹, similar to our case) typically resulted in direct penetration into cell, while higher concentration (160 μ g mL⁻¹) resulted in the endocytic uptake of NPs. ⁵³ To further explore the specific non-endocytic pathway of these NPs, it is necessary to perform a series of experiments to exclude endocytosis, such as the utilization of energy depletion mode and low temperature to inhibit endocytosis, which will be the next step of our future work.

The Au content of cells treated by NPs with different functionalization types was further quantified by ICP-MS. It was shown that the SPIO-Au-Py and SPIO-Au-Py-PCC-3 groups gained much higher Au content compared with the stand-alone SPIO-Au groups after 1 day and 2 days of incubation, while the SPIO-Au-RhB and SPIO-Au-RhB-PCC-2 groups gained lower Au content compared with the stand-alone SPIO-Au groups

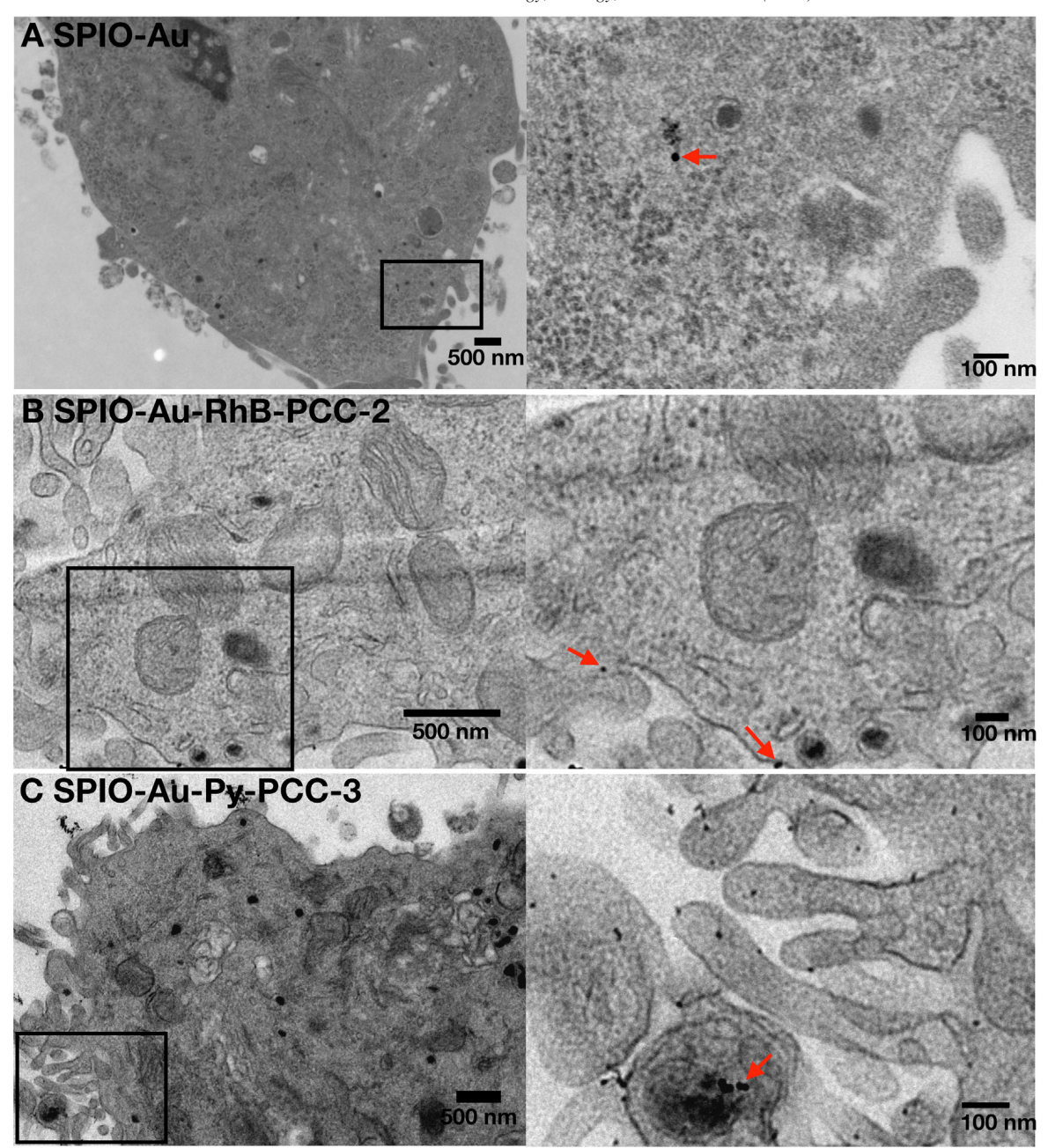


Figure 5. The TEM images showing the cellular uptake of PC-12 cells treated with (A) SPIO-Au, (B) SPIO-Au-RhB-PCC-2 and (C) SPIO-Au-Py-PCC-3 for 24 h. (The right parts were the enlarged images of areas in the black box in (A), (B) and (C).)

(Figure 6), indicating the enhanced NPs-cells interaction by Py-PEG-SH and PCC-3. It was also interesting to observe that the amount of Au of all groups reached the maximum value at 2 days of incubation, suggesting that almost all NPs interacted with cells at 2 days.

Cellular viability examination

To investigate whether or not the functionalization of NPs affected the cellular viability, the PC-12 cells treated with NPs were analyzed through flow cytometry. For up to 5 days of incubation, no significant reduction of cellular viability was observed for all NPs treated groups compared with the control,

indicating that the Py-PEG-SH, RhB-PEG-SH, PCC-2 and PCC-3 functionalization of NPs did not induce any significant toxicities on PC-12 cells (Figure 7). Instead, there was a slight increase of cell viability for groups treated with NPs at longer incubation time, i.e., 5 days. This may be explained by the promotional effect of SPIO-Au NPs on cell proliferation, which was reported before.³⁰

The drug loading and release capability of PCC-3 functionalized SPIO-Au NPs

It was previously demonstrated that both the electrostatic and hydrophobic interactions contribute to the guest binding of

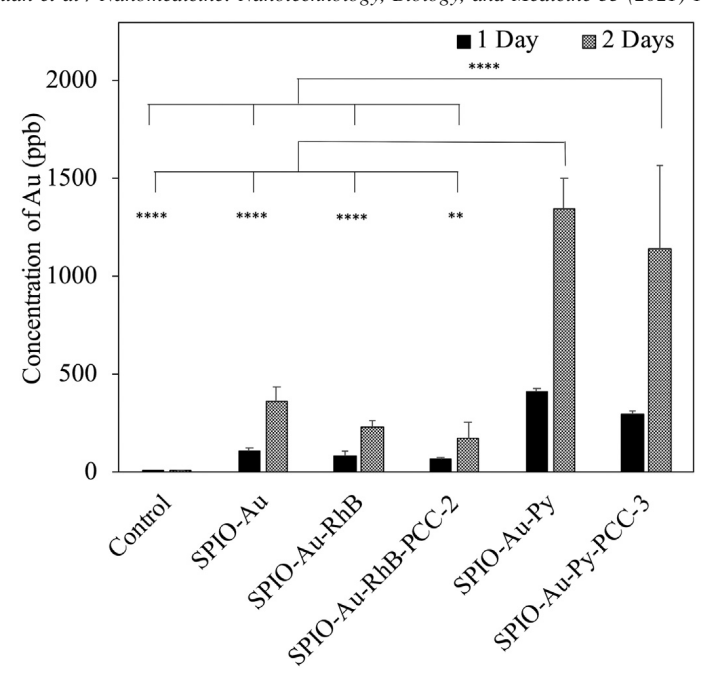


Figure 6. The relative absorbed amount of Au in PC-12 neuron-like cells treated with SPIO-Au NPs functionalized with Py-PEG-SH, RhB-PEG-SH, PCC-2 and PCC-3. Cells without NPs were used as the control group with nearly 0 Au absorption. *P < 0.05; **P < 0.01; ****P < 0.001; ****P < 0.0001. (Original data set is listed in Table S4.)

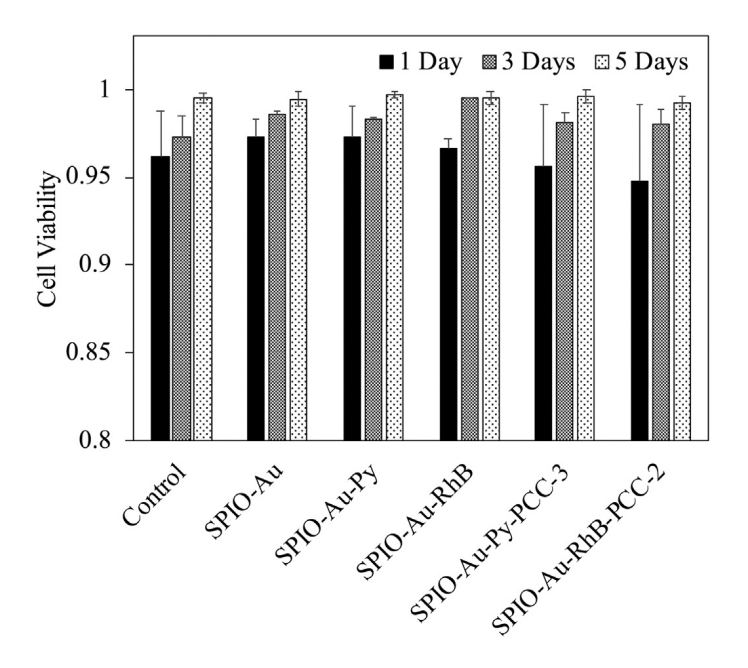


Figure 7. The cellular viability determined from flow cytometry for PC-12 neuron-like cells treated with SPIO-Au NPs with different types of functionalization. The cells without NPs were used as control group. *P < 0.05.

PCCs. ^{25–27} Different types of PCCs exhibited distinct structural and functional varieties for encapsulating different type of drug. Herein, we selected surface modified SPIO-Au-Py-PCC-3 NPs with positive net-charge (18 mV) and hydrophobic internal cavities for encapsulating the negatively charged moiety of RA. As a result, a significant reduction of the peak light absorbance was observed in the RA solution after removing the RA loaded SPIO-Au-Py-PCC-3 NPs compared with the RA solution before adding SPIO-

Au-Py-PCC-3 NPs, implying the successful encapsulation of RA into SPIO-Au-Py-PCC-3 NPs (Figure 8, A). The RA payload rate was estimated to be 13.505 µg/mg, indicating that about 13.505 µg of RA was loaded to every 1 mg of SPIO-Au-Py-PCC-3 NPs (Table 4). We then examined the release of RA, illuminated by 525 nm LED light. We observed that the release rate was much higher with the existence of LED illumination for 30 min from the starting point of drug release, compared with the control. The release of RA

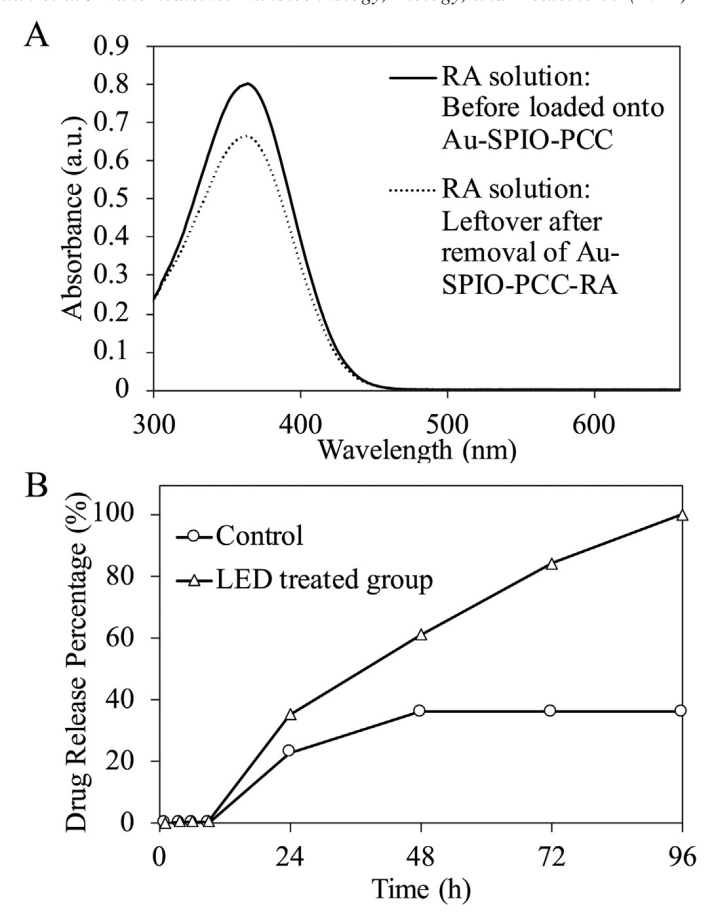


Figure 8. (A)The UV-vis light absorbance spectra of RA solution before adding SPIO-Au-Py-PCC-3 (red line) and the RA solution after removing the RA loaded SPIO-Au-Py-PCC-3 NPs(black line). (B) Accumulated release profile of RA in DMEM from SPIO-Au-Py-PCC-3 NPs.

Table 4
The drug loading characteristics of SPIO-Au-Py-PCC-3.

	SPIO-Au	RA	RA payload
	[mg]	[μg]	[μg/mg]
Mass composition of every 1 mL of drug loaded NPs	0.382	5.165	13.505

from NPs in DMEM with the LED illumination initiated as early as 1 h from the starting point of drug release, and reached 100% after 96 h, indicating a controlled and sustained release of RA from SPIO-Au-Py-PCC-3 NPs via light (Figure 8, *B*).

Discussion

In this work, we have developed a generalized nanocarrier by functionalizing SPIO-Au core-shell NPs with PCCs using the thiol-containing molecules (RhB/Py-PEG-SH) as bridges. SPIO-Au NPs (21 nm diameter) were synthesized according to our previous work which showed good *in-vitro* cellular viability on various cell lines including the PC-12 cells and MC-3T3 cells at the dosage of 10-80 μg mL⁻¹ without affecting the cell morphology. ^{29,30,41} Previous literature found that the surface functionalization or capping ligand may induce the toxicity of

Au NPs, such as cationic ligands protected NPs 54 and cetrimonium bromide-coated NPs. 55 However, whether or not the PCC functionalizations using RhB/Py-PEG-SH as bridges affect the toxicity of SPIO-Au NPs was still unknown. In this work, we were able to show that the Py-PEG-SH, RhB-PEG-SH, PCC-2 and PCC-3 functionalized SPIO-Au NPs did not induce significant toxicity in PC-12 cells at the concentration of 20 μg mL $^{-1}$, indicating the good biocompatibility of this nanocarrier.

The cellular internalization of NPs can be affected by the type of surface charges and functionalization groups of NPs. 56,57 The cellular uptake results revealed that the SPIO-Au-Py-PCC-3 and SPIO-Au-RhB-PCC-2 NPs could directly penetrate into cells through non-endocytic pathway, indicating their great potential as a nanocarrier for efficient intracellular drug delivery by avoiding the aggregation and restriction by the endosomes existing in the endocytic uptake pathway. 58 The relatively higher amount of Py-PEG-SH functionalized NPs that interacted with cells further indicated that the type of the bridge and PCCs affected the NPs-cells interaction and the cellular uptake efficiency. Since the uptake of NPs was mediated mainly by the nonspecific absorption of various serum proteins, ⁵⁹ it was hypothesized that there were more types of serum proteins absorbed onto the surfaces of Py-PEG-SH functionalized NPs, which allowed the higher amount of NPs that interacted with cells via multiple protein receptors.

Thanks to the inner cavity with different hydrophobicities and the adjustable net-charges, the proposed SPIO-Au-RhB-PCC-2 and SPIO-Au-Py-PCC-3 NPs possess the high potential to accommodate the needs of many kinds of drugs. For example, the SPIO-Au-RhB-PCC-2 NPs can be used to attract and encapsulate positively charged molecules because of the negative net-charge of PCC-2, while the SPIO-Au-Py-PCC-3 NPs can be used to attract and encapsulate the negatively charged hydrophobic drugs due to the positive net-charge and the stronger hydrophobicity of PCC-3. To demonstrate the ability of surface-charge tunable PCC-functionalized NPs for generalized drug delivery purpose, RA with hydrophobic nature and negatively charged moiety was chosen as the guest molecule. The surface charge modified SPIO-Au-Py-PCC-3 NPs with positive zeta potential were chosen as the drug carrier of RA. The high RA loading efficiency indicated the strong potential of SPIO-Au-Py-PCC-3 NPs as the drug carrier of RA and some other drugs, by adjusting the functional group, the surface charge and the hydrophobicity according to the property of guest molecules. The sustained RA release pattern suggested the potential of SPIO-Au-Py-PCC-3 NPs to minimize the rapid metabolization of RA in cells. However, we found that the drug release percentage for SPIO-Au-Py-PCC-3 NPs as control group was below 40% for up to 96 h which was far beyond the half-life of NPs with similar structures (29 h). 60 By running the drug release test under LED treatment, we found that the drug release rate can reach almost 100% for up to 96 h, which suggested the effect of LED on enhancing the drug release rate of this nanodelivery system. This controllable and sustainable RA release pattern could be triggered by depressing the hydrophobic interaction, accelerating the molecules diffusion, and enhancing the dissociation of PCC-3 structure. These effects were possibly induced by the plasmonic heat generated by SPIO-Au NPs with the stimulation of 525 nm LED light. 30 This is a very important feature for the design and in vivo test of nanodelivery system to have controllable and sustainable drug release pattern within the time-frame of the NPs' half-lives, since the 100% release before the excretion of NPs from the animal body is favored. It is expected that by adjusting the LED light intensities, the drug release rate at a certain time period can be further modified to accommodate their half-lives. This will be our future objective to study the effect of different LED intensity on drug release characteristics and the in vivo drug delivery of the nanodelivery system. Additionally, the pH-sensitive nature of PCCs observed from our previous work also supported another controllable parameter for this nanocarrier. $^{26-28}$ Considering the composition of the nanocarrier, it is not only a bio-compatible agent and a promising intracellular targeting tool, but also a potential remotely-controllable mobile medical device for in vitro and in vivo multimodal medical applications to utilize the magnetoplasmonic nature of SPIO-Au NPs.

In summary, this study reported a novel smart nanocarrier composed by PCCs functionalized SPIO-Au NPs using thiol molecules as bridges. The functionalization of SPIO-Au NPs with thiol groups and two types of PCCs (PCC-2 and PCC-3) and their excellent biocompatibility at the concentration of 20 µg mL⁻¹ were demonstrated. The cellular uptake evaluation revealed the intracellular targeting of PCC-2 and PCC-3 functionalized NPs

via the direct penetration across the cell membranes. The significantly higher amount of cells-interacted NPs with Py-PEG-SH functionalization was observed. The drug loading capability of surface-charge modified SPIO-Au-Py-PCC-3 NPs as smart nanocarriers was demonstrated by observing a payload of 13.505 µg/mg. Particularly, the LED-light controlled and enhanced RA release was observed on this nanocarrier with a sustainable 100% release for up to 96 h.

Acknowledgments

This work was kindly supported by the U.S. National Science and Foundation (CAREER grant number 1751435, Y.W. GCR grant number 2021081, Y.W.), by the U.S. National Institute of General Medical Sciences (grant number R01GM110137, J.-P.P.) and by the Cancer Prevention and Research Institute of Texas (grant number RP190655, J.-P.P.).

Appendix A. Supplementary data

Supplementary data to this article can be found online at https://doi.org/10.1016/j.nano.2021.102392.

References

- Liu YY, Yang XY, Li Z, Liu ZL, Cheng D, Wang Y, et al. Characterization of polyethylene glycol-polyethyleneimine as a vector for alpha-synuclein siRNA delivery to PC12 cells for Parkinson's disease. CNS Neurosci Ther 2014;20:76-85.
- Lu XC, Zheng JY, Tang LJ, Huang BS, Li K, Tao Y, et al. MiR-133b promotes neurite outgrowth by targeting RhoA expression. *Cell Physiol Biochem* 2015;35:246-58.
- Garbayo E, Ansorena E, Lana H, del Mar Carmona-Abellan M, Marcilla I, Lanciego JL, et al. Brain delivery of microencapsulated GDNF induces functional and structural recovery in parkinsonian monkeys. *Biomaterials* 2016;110:11-23.
- Herrán E, Requejo C, Ruiz-Ortega JA, Aristieta A, Igartua M, Bengoetxea H, et al. Increased antiparkinson efficacy of the combined administration of VEGF-and GDNF-loaded nanospheres in a partial lesion model of Parkinson's disease. *Int J Nanomedicine* 2014;9:2677.
- Rodríguez-Nogales C, Garbayo E, Carmona-Abellán MM, Luquin MR, Blanco-Prieto MJ. Brain aging and Parkinson's disease: new therapeutic approaches using drug delivery systems. *Maturitas* 2016;84:25-31.
- Wohlfart S, Gelperina S, Kreuter J. Transport of drugs across the bloodbrain barrier by nanoparticles. *J Control Release* 2012;161:264-73.
- Satish A, Korrapati PS. Tailored release of triiodothyronine and retinoic acid from a spatio-temporally fabricated nanofiber composite instigating neuronal differentiation. *Nanoscale* 2017;9:14565-80.
- Esteves M, Cristóvão AC, Saraiva T, Rocha SM, Baltazar G, Ferreira L, et al. Retinoic acid-loaded polymeric nanoparticles induce neuroprotection in a mouse model for Parkinson's disease. *Front Aging Neurosci* 2015;7:20.
- Wu H, Zhao J, Fu B, Yin S, Song C, Zhang J, et al. Retinoic acid-induced upregulation of miR-219 promotes the differentiation of embryonic stem cells into neural cells. *Cell Death Dis* 2017;8e2953.
- Tozaki-Saitoh H, Koizumi S, Sato Y, Tsuda M, Nagao T, Inoue K. Retinoic acids increase P2X2 receptor expression through the 5'flanking region of P2rx2 gene in rat phaeochromocytoma PC-12 cells. *Mol Pharmacol* 2006;70:319-28.
- Maia J, Santos T, Aday S, Agasse F, Cortes L, Malva JO, et al. Controlling the neuronal differentiation of stem cells by the intracellular delivery of retinoic acid-loaded nanoparticles. ACS Nano 2010;5:97-106.

- Hu J, Liu Y-F, Wu C-F, Xu F, Shen Z-X, Zhu Y-M, et al. Long-term efficacy and safety of all-trans retinoic acid/arsenic trioxide-based therapy in newly diagnosed acute promyelocytic leukemia. *Proc Natl Acad Sci* 2009;106:3342-7.
- Mukherjee S, Date A, Patravale V, Korting HC, Roeder A, Weindl G. Retinoids in the treatment of skin aging: an overview of clinical efficacy and safety. *Clin Interv Aging* 2006;1:327.
- Santos T, Ferreira R, Maia J, Agasse F, Xapelli S, Ls Cortes, et al. Polymeric nanoparticles to control the differentiation of neural stem cells in the subventricular zone of the brain. ACS Nano 2012;6:10463-74.
- Ferreira R, Fonseca MC, Santos T, Sargento-Freitas J, Tjeng R, Paiva F, et al. Retinoic acid-loaded polymeric nanoparticles enhance vascular regulation of neural stem cell survival and differentiation after ischaemia. *Nanoscale* 2016;8:8126-37.
- Yalçın S, Erkan M, Ünsoy G, Parsian M, Kleeff J, Gündüz U. Effect of gemcitabine and retinoic acid loaded PAMAM dendrimer-coated magnetic nanoparticles on pancreatic cancer and stellate cell lines. *Biomed Pharmacother* 2014;68:737-43.
- Jeong Y-I, Kang M-K, Sun H-S, Kang S-S, Kim H-W, Moon K-S, et al. All-trans-retinoic acid release from core-shell type nanoparticles of poly (ε-caprolactone)/poly (ethylene glycol) diblock copolymer. *Int J Pharm* 2004;273:95-107.
- Saraiva C, Praça C, Ferreira R, Santos T, Ferreira L, Bernardino L. Nanoparticle-mediated brain drug delivery: overcoming blood-brain barrier to treat neurodegenerative diseases. *J Control Release* 2016;235:34-47.
- Boto C, Quartin E, Cai Y, Martín-Lorenzo A, Cenador MBG, Pinto S, et al. Prolonged intracellular accumulation of light-inducible nanoparticles in leukemia cells allows their remote activation. *Nat Commun* 2017;8:1-13.
- Santos T, Ferreira R, Quartin E, Boto C, Saraiva C, Bragança J, et al. Blue light potentiates neurogenesis induced by retinoic acid-loaded responsive nanoparticles. *Acta Biomater* 2017;59:293-302.
- Rao S, Chen R, LaRocca AA, Christiansen MG, Senko AW, Shi CH, et al. Remotely controlled chemomagnetic modulation of targeted neural circuits. *Nat Nanotechnol* 2019;14:967-73.
- Park J, Jin C, Lee S, Kim JY, Choi H. Magnetically actuated degradable microrobots for actively controlled drug release and hyperthermia therapy. Adv Healthc Mater 2019;8:1900213.
- Sudik AC, Millward AR, Ockwig NW, Côté AP, Kim J, Yaghi OM. Design, synthesis, structure, and gas (N2, Ar, CO2, CH4, and H2) sorption properties of porous metal-organic tetrahedral and heterocuboidal polyhedra. J Am Chem Soc 2005;127:7110-8.
- Sato S, Iida J, Suzuki K, Kawano M, Ozeki T, Fujita M. Fluorous nanodroplets structurally confined in an organopalladium sphere. *Science* 2006;313:1273-6.
- Kaphan DM, Levin MD, Bergman RG, Raymond KN, Toste FD. A supramolecular microenvironment strategy for transition metal catalysis. *Science* 2015;350:1235-8.
- Fang Y, Lian X, Huang Y, Fu G, Xiao Z, Wang Q, et al. Investigating subcellular compartment targeting effect of porous coordination cages for enhancing cancer nanotherapy. Small 2018;14:1802709.
- Zheng Y-R, Suntharalingam K, Johnstone TC, Lippard SJ. Encapsulation of Pt (IV) prodrugs within a Pt (II) cage for drug delivery. *Chem Sci* 2015;6:1189-93.
- Samanta SK, Moncelet D, Briken V, Isaacs L. Metal-organic polyhedron capped with cucurbit [8] uril delivers doxorubicin to cancer cells. J Am Chem Soc 2016;138:14488-96.
- Yuan M, Wang Y, Qin Y-X. Promoting neuroregeneration by applying dynamic magnetic fields to a novel nanomedicine: superparamagnetic iron oxide (SPIO)-gold nanoparticles bounded with nerve growth factor (NGF). Nanomedicine: NBM 2018;14:1337-47.
- Yuan M, Wang Y, Qin Y-X. Engineered nanomedicine for neuroregeneration: light emitting diode-mediated superparamagnetic iron oxide-gold core-shell nanoparticles functionalized by nerve growth factor. *Nanomedicine: NBM* 2019;21:102052.

- Zhang S, Qi Y, Yang H, Gong M, Zhang D, Zou L. Optimization of the composition of bimetallic core/shell Fe2O3/Au nanoparticles for MRI/ CT dual-mode imaging. J Nanopart Res 2013;15:1-9.
- Na HB, Song IC, Hyeon T. Inorganic nanoparticles for MRI contrast agents. Adv Mater 2009;21:2133-48.
- Yuan M, Wang Y, Hwang D, Longtin JP. Thermocouple-tip-exposing temperature assessment technique for evaluating photothermal conversion efficiency of plasmonic nanoparticles at low laser power density. *Rev Sci Instrum* 2019;90094902.
- Yoffe S, Leshuk T, Everett P, Gu F. Superparamagnetic iron oxide nanoparticles (SPIONs): synthesis and surface modification techniques for use with MRI and other biomedical applications. *Curr Pharm Des* 2013;19:493-509.
- 35. Nam SY, Ricles LM, Suggs LJ, Emelianov SY. Imaging strategies for tissue engineering applications. *Tissue Eng Part B Rev* 2014;21:88-102.
- Lalande C, Miraux S, Derkaoui SM, Mornet S, Bareille R, Fricain J-C, et al. Magnetic resonance imaging tracking of human adipose derived stromal cells within three-dimensional scaffolds for bone tissue engineering. Eur Cell Mater 2011;21e54.
- Kawazoe N, Chen G. Gold nanoparticles with different charge and moiety induce differential cell response on mesenchymal stem cell osteogenesis. *Biomaterials* 2015;54:226-36.
- Xu Z, Hou Y, Sun S. Magnetic core/shell Fe3O4/Au and Fe3O4/Au/Ag nanoparticles with tunable plasmonic properties. *J Am Chem Soc* 2007:129:8698-9.
- Connor EE, Mwamuka J, Gole A, Murphy CJ, Wyatt MD. Gold nanoparticles are taken up by human cells but do not cause acute cytotoxicity. Small 2005;1:325-7.
- Albanese A, Chan WCW. Effect of gold nanoparticle aggregation on cell uptake and toxicity. ACS Nano 2011;5:5478-89.
- Yuan M, Wang Y, Qin YX. SPIO-Au core–shell nanoparticles for promoting osteogenic differentiation of MC3T3-E1 cells: concentrationdependence study. *J Biomed Mater Res A* 2017;105:3350-9.
- Mahmoudi M, Sant S, Wang B, Laurent S, Sen T. Superparamagnetic iron oxide nanoparticles (SPIONs): development, surface modification and applications in chemotherapy. Adv Drug Deliv Rev 2011;63:24-46.
- Baranes K, Shevach M, Shefi O, Dvir T. Gold nanoparticle-decorated scaffolds promote neuronal differentiation and maturation. *Nano Lett* 2015;16:2916-20.
- Papastefanaki F, Jakovcevski I, Poulia N, Djogo N, Schulz F, Martinovic T, et al. Intraspinal delivery of polyethylene glycol-coated gold nanoparticles promotes functional recovery after spinal cord injury. *Mol Ther* 2015;23:993-1002.
- Wei M, Li S, Yang Z, Zheng W, Le W. Gold nanoparticles enhance the differentiation of embryonic stem cells into dopaminergic neurons via mTOR/p70S6K pathway. *Nanomedicine* 2017;12:1305-17.
- Zhang Q, Kim D, Li L, Patel S, Duhamel J. Surfactant structuredependent interactions with modified starch nanoparticles probed by fluorescence spectroscopy. *Langmuir* 2019;35:3432-44.
- 47. Barry NPE, Therrien B. *Pyrene: the guest of honor. Sadjadi S, Organic nanoreactors.* 1st ed. Academic Press; 2016421-61.
- Schneider G, Decher G, Nerambourg N, Praho R, Werts MHV, Blanchard-Desce M. Distance-dependent fluorescence quenching on gold nanoparticles ensheathed with layer-by-layer assembled polyelectrolytes. *Nano Lett* 2006;6:530-6.
- Chou LYT, Chan WCW. Fluorescence-tagged gold nanoparticles for rapidly characterizing the size-dependent biodistribution in tumor models. Adv Healthc Mater 2012;1:714-21.
- Geiser M, Rothen-Rutishauser B, Kapp N, Schürch S, Kreyling W, Schulz H, et al. Ultrafine particles cross cellular membranes by nonphagocytic mechanisms in lungs and in cultured cells. *Environ Health Perspect* 2005;113:1555-60.
- Rothen-Rutishauser BM, Schürch S, Haenni B, Kapp N, Gehr P. Interaction of fine particles and nanoparticles with red blood cells visualized with advanced microscopic techniques. *Environ Sci Technol* 2006;40:4353-9.

- Li Z, Zhang Y, Zhu D, Li S, Yu X, Zhao Y, et al. Transporting carriers for intracellular targeting delivery via non-endocytic uptake pathways. *Drug Deliv* 2017;24:45-55.
- Mustafa T, Watanabe F, Monroe W, Mahmood M, Xu Y, Saeed LM, et al. Impact of gold nanoparticle concentration on their cellular uptake by MC3T3-E1 mouse osteoblastic cells as analyzed by transmission electron microscopy. *J Nanomed Nanotechnol* 2011;2:1000118.
- Goodman CM, McCusker CD, Yilmaz T, Rotello VM. Toxicity of gold nanoparticles functionalized with cationic and anionic side chains. *Bio-conjug Chem* 2004;15:897-900.
- Khlebtsov N, Dykman L. Biodistribution and toxicity of engineered gold nanoparticles: a review of in vitro and in vivo studies. *Chem Soc Rev* 2011;40:1647-71.

- Lin J, Alexander-Katz A. Cell membranes open "doors" for cationic nanoparticles/biomolecules: insights into uptake kinetics. ACS Nano 2013;7:10799-808.
- Lin J, Zhang H, Chen Z, Zheng Y. Penetration of lipid membranes by gold nanoparticles: insights into cellular uptake, cytotoxicity, and their relationship. ACS Nano 2010;4:5421-9.
- 58. Nativo P, Prior IA, Brust M. Uptake and intracellular fate of surface-modified gold nanoparticles. *ACS Nano* 2008;**2**:1639-44.
- Chithrani BD, Ghazani AA, Chan WCW. Determining the size and shape dependence of gold nanoparticle uptake into mammalian cells. *Nano Lett* 2006;6:662-8.
- Perrault SD, Walkey C, Jennings T, Fischer HC, Chan WCW. Mediating tumor targeting efficiency of nanoparticles through design. *Nano Lett* 2009;9:1909-15.